High-speed imaging of light-induced photoreceptor microsaccades in compound eyes

Joni Kemppainen[1], Neveen Mansour[1], Jouni Takalo[1] & Mikko Juusola[1,2*]

[1]Department of Biomedical Science, University of Sheffield, Sheffield S10 2TN, UK
[2]National Key Laboratory of Cognitive Neuroscience and Learning, Beijing, Beijing Normal University, Beijing 100875, China.

*** Correspondence:** Mikko Juusola
m.juusola@sheffield.ac.uk

Keywords: photoreceptor, open rhabdom, fused rhabdom, microsaccade, *Drosophila*, deep pseudopupil, goniometry, hyperacuity, active sampling, active vision

Abstract

Inside compound eyes, photoreceptors contract to light changes[1-3], sharpening retinal images of the moving world in time[2]. Current methods to measure these so-called photoreceptor microsaccades in living insects are spatially limited and technically challenging[1, 2]. Here, we present goniometric high-speed deep pseudopupil (GHS-DPP) microscopy to assess how the rhabdomeric insect photoreceptors and their microsaccades are organised across the compound eyes. This method enables non-invasive rhabdomere orientation mapping, whilst their microsaccades can be locally light-activated, revealing the eyes' underlying active sampling motifs. By comparing the microsaccades in wild-type *Drosophila*'s open rhabdom eyes[4] to *spam*-mutant eyes, reverted to an ancestral fused rhabdom state[5, 6], we show how two different eye types sample light information. These results show different ways how vision converts space into time[2, 3, 7-11], and highlight how compound eyes and their active sampling can evolve with insects' visual needs.

Introduction

Because the insect compound eyes extend from the rigid head exoskeleton, appearing stationary to an outside observer, it was long assumed that their inner workings would also be static. Therefore, as the eyes' ommatidial faceting sets their photoreceptor spacing, it was deduced that the compound eyes could only sample a pixelated low-resolution image of the world[12-14].

However, recent results on the *Drosophila* compound eyes are now replacing this stationary viewpoint with a new concept of ultrafast morphodynamic active sampling[2, 3]. Sophisticated experiments have revealed how photoreceptor microsaccades *locally*[2, 3] and intraocular muscle contractions *globally*[2, 9, 15] move, stretch and recoil intraommatidial optical structures, improving vision morphodynamically. The *local* microsaccades increase sampling resolution in space and sharpen light input in time for super-resolution vision[2]. And, with the left and right eye photoreceptor pairs generating mirror-symmetric microsaccades, this active sampling further expands the flies' hyperacute stereopsis[3]. Conversely, the intraocular muscle contractions shift one eye's sampling matrix *globally* regarding the other eye. These retinal vergence movements, which also happen underneath the eyes' rigid ommatidial lens cover, hidden from the outside view, combat adaptive perceptual fading by refreshing gaze[2, 15] and may contribute to attentive saccadic viewing and object tracking[9].

Minute photomechanical photoreceptor contractions (<~200 nm) were first measured in *ex vivo Drosophila* preparations using atomic force microscopy (AMF)[1]. Initially, these movements, caused by PIP_2 cleavage in the microvillar photoreceptor membrane[1, 16], were thought to be too small to alter the photoreceptors' light input[1]. However, later live-microscopy experiments, using the cornea neutralisation method[17], showed that *ex vivo* AFM underestimates the size of the lateral rhabdomere

movements[2]. Intense light modulation *in vivo* could move an R1-R6 rhabdomere about its width (~1,400 nm) sideways, and with similar microsaccades also occurring in synaptically decoupled photoreceptors[2], the results demonstrated active sampling inside an ommatidium for the first time[2]. Unfortunately, both these methods are technically demanding and spatially limiting and thus ill-suited for mapping the microsaccade movement sizes and directions across the left and right compound eyes.

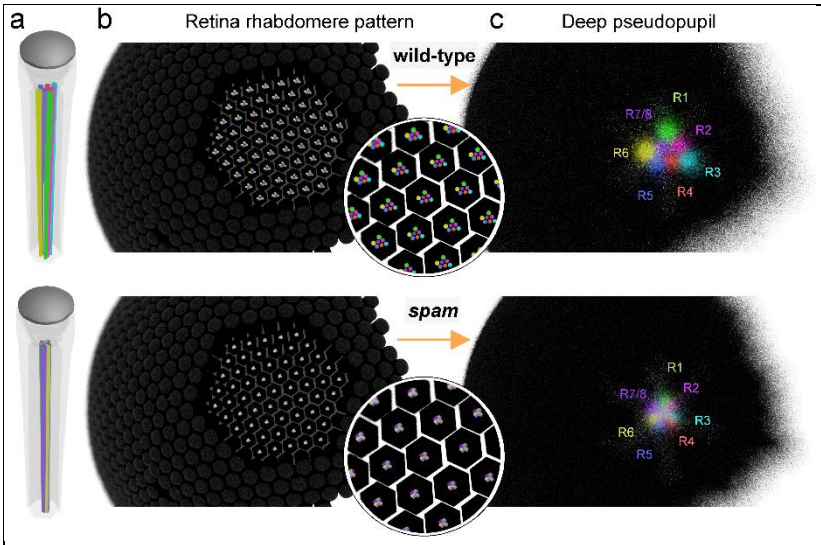

Fig. 1 | Deep pseudopupil (DPP) in the wild-type and *spam*, and rhabdomere orientation. a, The *Drosophila* compound eye comprises ~750 ommatidia, each having a light focusing facet lens and eight photoreceptors; with their light-sensitive parts, the rhabdomeres (coloured), protruding centrally. **b**, Computer graphics (CG) models of the open wild-type and fused *spam* rhabdoms; here shown for their left eye's southern hemisphere. **c**, The CG-model simulated DPP image appears as a magnified "virtual" image of the rhabdomere pattern. In the *spam*, DPP appears as a tiny bright disc. The R1-R7/8 rhabdomere colouring of the corresponding photoreceptors indicates their relative locations.

In the compound eyes, an optical phenomenon called the deep pseudopupil (DPP) arises from the regular arrangement of ommatidia (**Fig. 1**), each containing R1-R7/8 photoreceptors in which open rhabdomeres act as waveguides[18] (**Fig. 1a**). By focussing a microscope's image plane below the eye's outer surface (**Fig. 1b**), virtual images of several ommatidia's R1-R7/8 rhabdomere patterns become superimposed (**Fig. 1c**), revealing their stereotypical yet magnified trapezoid arrangement. Thus, DPP microscopy offers a versatile, non-invasive method to observe retinal tissue in living flies and other insects. First, to observe a well-defined, clear DPP pattern in dipteran eyes requires precisely organised rhabdomeres across the neighbouring ommatidia[19], and DPP microscopy with epi-illumination[20, 21] (frontally, through the eye optics) has been used to study retinal degeneration that breaks this order[22-24]. Second, because the rhabdomeres contributing to the DPP image are those facing the observer, the DPP microscopy provides the "gold standard" measure for the binocular overlap over the left and right compound eyes[25-27]. Finally, because any lateral retinal tissue movement shifts the DPP similarly, DPP microscopy can be used to investigate how the eye-muscle-induced retinal micromovements shift the photoreceptors' receptive fields[28].

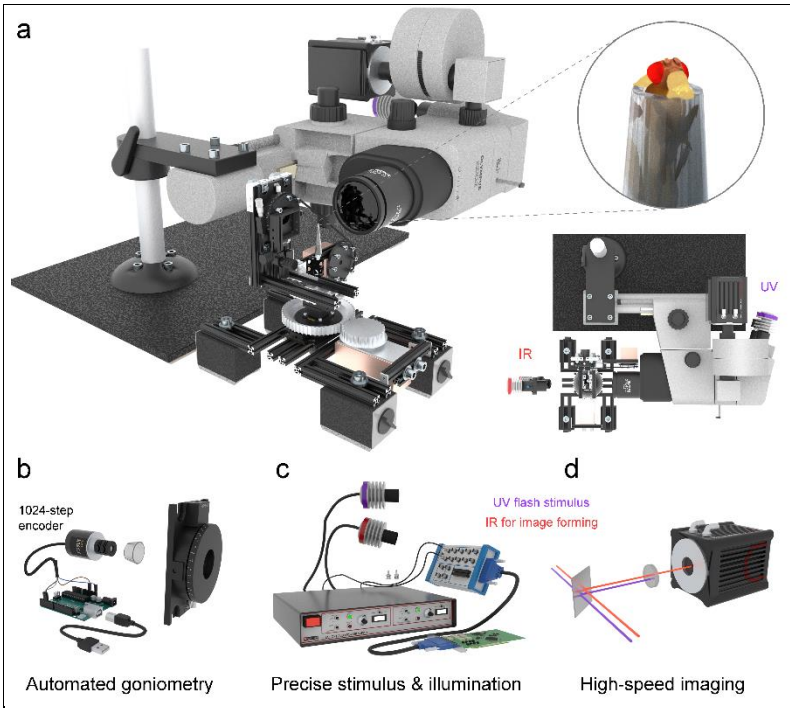

Fig. 2 | Goniometric high-speed deep pseudopupil (GHS-DPP) imaging system. a, Its integral parts are a sideways mounted stereo microscope with a high-speed (100-1,000 fps) digital camera and a goniometric rotation stage system. *Drosophila* eyes are imaged under the antidromic dual infrared illumination, invisible to the flies[2, 29]. Photoreceptor microsaccades are activated by ultraviolet (UV) light stimulation, delivered through the ocular slot system. **b**, The fly's x/y-rotations are read using a 1024-step rotary encoder and an Arduino board. **c**, The high-power LEDs and the camera were controlled over the BNC interface. **d**, An infrared (IR) passing but UV blocking optical filter in the front of the camera decouples the UV-stimulus from the imaging pathway. See **Supplementary Video 1**.

Here, we present a novel goniometric high-speed deep pseudopupil (GHS-DPP) microscopy (**Fig. 2**) with invisible (850 nm) infrared back-illumination, developed to study active sampling in insect compound eyes. We use it to measure the microsaccade dynamics and directions in wild-type *Drosophila*, possessing the archetypical open rhabdom dipteran eyes (**Fig. 1**, above), and transgenic *spam* null-mutants, in which rhabdomeres fail to separate (**Fig. 1**, bellow), forming an ancestral, fused rhabdom (apposition) eye[30]. Our results show that active sampling by photoreceptor microsaccades occurs both in the open and fused rhabdom eyes. We analyse these phenotypes' functional similarities and differences and discuss what these results could mean for the evolution of compound eyes and insect vision in general, with many insect species having apposition eyes[31].

Results

We first inspected the wild-type and *spam* flies' DPP patterns in still images taken under antidromic infrared illumination in perceptual darkness (**Fig. 3**). Characteristically, the wild-type DPP image merged the neighbouring ommatidia's R1-R7/8 rhabdomere images into a classic trapezoid pattern of seven small bright discs (**Fig. 3a**). In contrast, the *spam* DPP appeared as a tiny bright disc (**Fig. 3d**). These different DPP patterns were entirely expected, as they directly follow the deep pseudopupil theory[19] and our CG-modelling (**Fig. 1**).

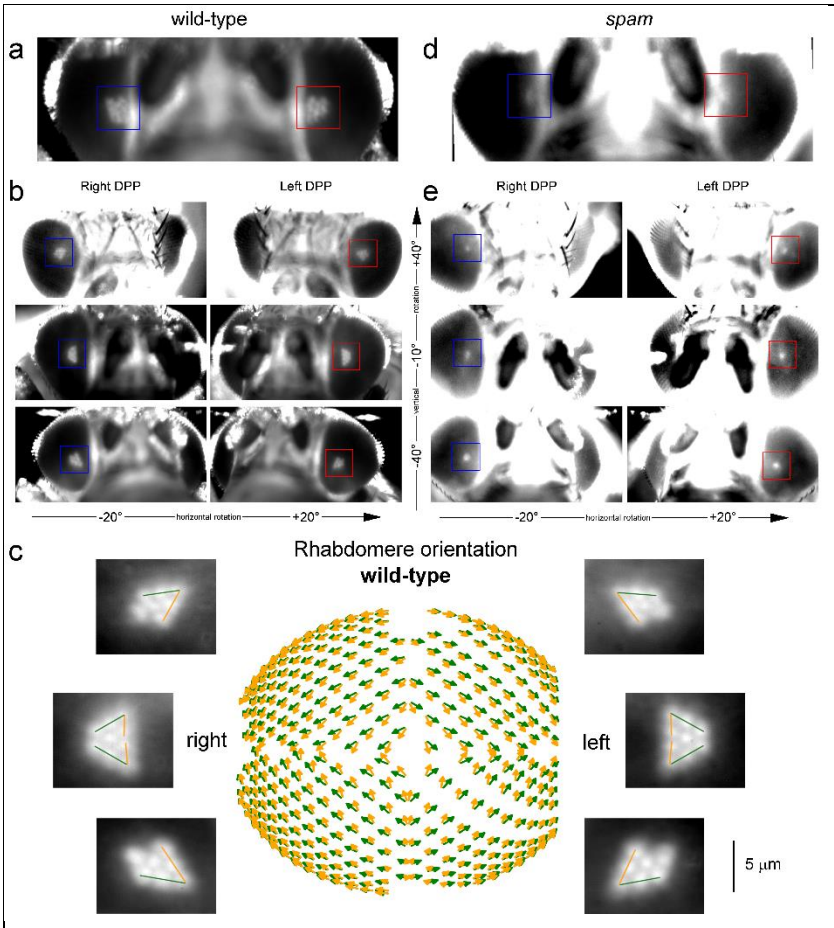

Fig. 3 | Wild-type and *spam* DPP imaged by the 850 nm GHS-DPP microscopy. a, Forward-facing wild-type eyes (horizontal rotation = 0 °) with the red and blue square boxes indicating their left and right DPPs, respectively. **b**, Wild-type eyes, viewed on the dorsal side (1st row), at the midline (2nd row), and on the ventral side (3rd row), reveal their DPPS ventral-dorsal symmetry. **c**, The wild-type rhabdomere orientation across the left and right eyes as mapped with the GHS-DPP microscopy. The green lines indicate the R1-R2-R3 rhabdomere axes, and the yellow lines the R3-R4-R5 axes. R1-R7/8 rhabdomeres rotate systematically with changing eye location, producing concentrically-expanding diamonds-patterns[3], highlighting the characteristic right-left eye and north-south (dorsal-ventral) hemisphere mirror-symmetricity. **d**, The left and right eye *spam* DPPs appear circular-symmetric discs and are more oversaturated due to their eyes' lighter pigmentation. (**e**) *spam* eyes with their DPPs, viewed on the dorsal side, at the midline, and on the ventral side.

The infrared GHS-DPP microscopy made it straightforward to record, measure and map the DPP pattern changes across the eyes. In the wild-type, the left and right eyes' DPPs are mirror-symmetric: shown in the binocular upper-frontal view (**Fig. 3a**; the blue and red boxes highlight their right and left DPPs, respectively). Interestingly, the north and south hemispheres of the eye also have mirror-symmetric DPP patterns[32] but fuse at the equator (mid-line) to form larger elongated triangle shapes (**Fig. 3b**). The DPP orientation, as the angular rotation between R3-R2-R1 rhabdomeres (yellow line) and R3-R4-R5 rhabdomeres (green), shifts between nearby eye locations in regular small steps, generating the left and right eyes' mirror-symmetric global map (**Fig. 3c**). In this global map, local DPP alignments follow a concentrically expanding diamond-shaped pattern. Therefore, the underlying developmentally rotated R1-R7/8 rhabdomere orientations at each eye position align with the frontally expanding optic flow field[3]. On the contrary, in the *spam* mutant, because their DPPs appear as homogeneous circular or oval discs (**Fig. 3d**), neither such gradual rotations nor their left-right and north-south divisions were readily observable (**Fig. 3e**).

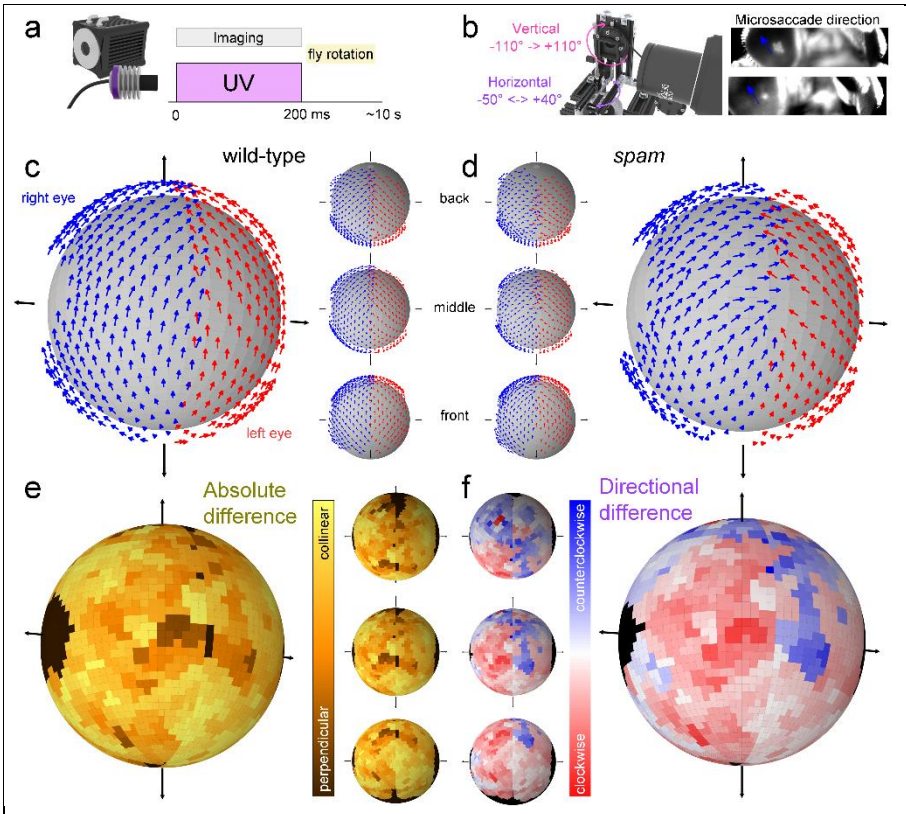

Fig. 4 | DPP microsaccades across the left and right wild-type and *spam* eyes. a, During the 200 ms UV flash, the camera recorded the DPP microsaccades 100 frames-per-second. **b**, After each flash, the fly was rotated, recording approximately 200 locations on the left and right eyes. **c**, Mean microsaccade vector map of wild-type flies (N = 5; the arrows indicate eye-location-specific normalised microsaccade directions). The small insets show the dorsal, the anterior and the ventral vector map views from the top to bottom. **d**, Mean microsaccade vector map of spam files (N=5) appears similar to the wild-type but only slightly noisier. **e**, Absolute difference plot of the wild-type and *spam* vector maps show that the wild-type and *spam* vector maps are mostly collinear. **f**, On the anterior eye regions, the directional difference graph suggests that the *spam* right eye microsaccades are clockwise-rotated and the left eye microsaccades counterclockwise-rotated compared to the wild-type (as viewed from outside). See **Supplementary Video 2** and **3**.

Next, while imaging the eyes' DPPs, we recorded their ultrafast (time-to-peak <100 ms) photomechanical microsaccades to 200 ms ultraviolet (365 nm) bright light flashes (**Supplementary Video 2**). We mapped these DPP microsaccades and their directions from about 200 distinct locations over the left and right eyes (**Fig. 4a** and **b**). In the wild-type, the DPP microsaccades moved approximately from back-to-front or south-to-north, depending on the eye region (**Fig. 4c**). But we did not image the DPP microsaccade relaxation phase, which occurs during light decrements (darkening), moving slower and in opposite directions to the activation phase[2].

Remarkably, we discovered that the fused rhabdom *spam* flies also showed clear ultrafast DPP microsaccades, which generally moved along similar directions to those of wild-type (**Fig. 4d**). Furthermore, we calculated the absolute difference in the rotation of the microsaccades between the wild-type and *spam* flies and found their resulting global maps broadly similar (**Fig. 4e**; **Supplementary Video 3**). However, in a more detailed inspection, the *spam* left eye DPP microsaccades on the anterior parts showed slightly more counterclockwise rotation and the right eye DPP microsaccades slightly more clockwise rotation than the wild-type (**Fig. 4f**).

These results demonstrate active sampling - by photomechanical photoreceptor microsaccades - happening in fused rhabdom eyes. Moreover, since the wild-type microsaccade directions (their forward-and-back movement axes) align with their R1-R2-R3 rhabdomere axis (**Fig. 3c**, yellow arrows)[3], it seems highly likely that the *spam* R1-R8 photoreceptors inside the ommatidia would also rotate in an eye-position-dependent manner, resulting in the ventral-dorsal hemispheric DPP mirroring. However, we could not directly confirm this from the round and oval *spam* DPP images (**Fig. 3e**). Nevertheless, in both phenotypes, the photoreceptors' active sampling makes their receptive

fields scan the world in their eye-location-specific directions, broadly matching the flies' concentrically expanding optic flow field during the forward locomotion[3].

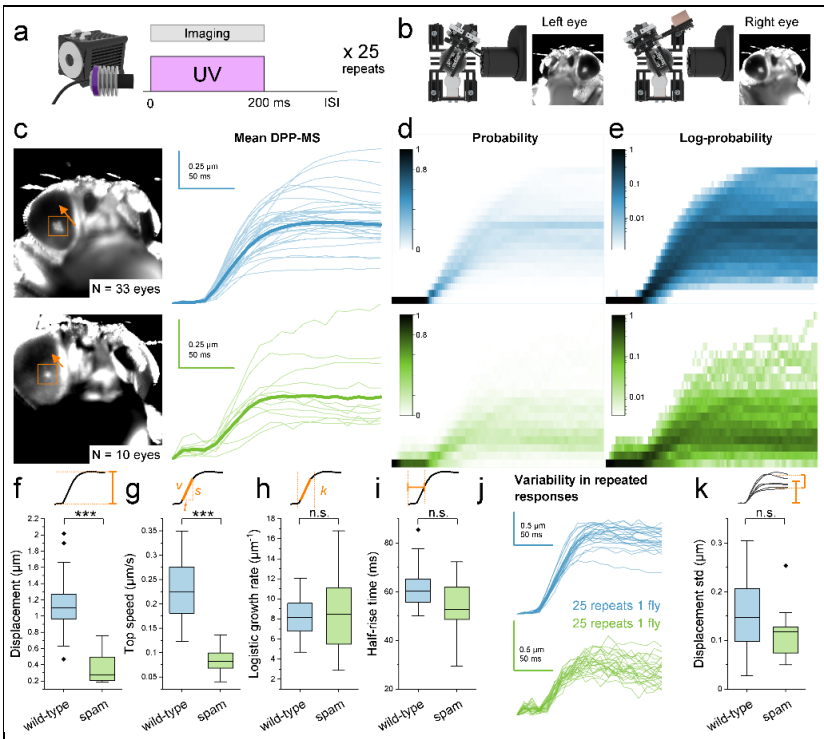

Fig. 5 | DPP microsaccade kinematics in the wild-type and *spam*. a, In the local recordings, the UV flash was repeated 25 times every inter-stimulus interval (ISI). **b**, These experiments were done at one fixed location in each eye. **c**, Mean rhabdomere displacements in the wild-type (1st row) and *spam* (2nd row) appear similar in shape but are smaller in *spam*. **d-e**, The probability plots, containing the separate (single) responses, indicate that the photoreceptor microsaccades occur over a predictable but variable range. **f-j**, The overall displacement, the top speed, the logistic growth factor and the half-rise time, respectively, in the wild-type and *spam* (Welch's t-test; $p = 1.1 \times 10^{-11}$, $p = 7.0 \times 10^{-14}$, $p = 0.11$, $p = 0.73$). **j**, The DPP microsaccade responses of one selected wild-type and one *spam* show variability in repeated responses that may indicate purposeful modulation. **k**, Quantified displacement standard deviations (std) for all the wild-type and *spam* flies do not differ statistically (Welch's t-test; $p = 0.076$).

After the global characterisation, we recorded local DPP microsaccades from the fixed left and right eye locations (±28° horizontal, -37° vertical), repeating the recordings 25 times to obtain more robust estimates and additional statistics (**Fig. 5a** and **b**). Qualitatively, both the wild-type and *spam* had similar looking microsaccade kinematics, but the overall displacement amplitudes appeared much smaller in *spam* (**Fig. 5c-e**). Displacement measurements confirmed that the *spam* DPP microsaccades were indeed smaller than the wild-type (**Fig. 5f**). Similarly, the *spam* flies' calculated maximum microsaccade activation speed was significantly slower (**Fig. 5g**). However, these phenotypes' logarithmic growth factors during the activation phase did not differ statistically (**Fig. 5h**), meaning that the *spam* DPP microsaccades' slower speed resulted from their shorter travelling distance but not from changes in their duration. Accordingly, there was no significant change in the half-rise times (**Fig. 5i**). The similar logarithmic growth factors and half-rise times suggest that the likely photomechanical cause of the DPP microsaccades, the PIP_2 cleavage from the microvillar membrane during phototransduction[1], is unaffected by the *spam* mutation. Overall, these results show that the *spam* flies have similar microsaccade kinematics as the wild-type but are only smaller.

Finally, we inspected individual flies' DPP microsaccade variations to the 25 times repeated light flashes. A qualitative comparison between the selected wild-type and *spam* flies showed that most variation occurs in the total displacement; that is, how far the DPP and the rhabdomeres travel during the microsaccade activation phase (**Fig. 5j**). Furthermore, we found no difference between their DPP displacements' standard deviations (**Fig. 5k**), indicating similar intrinsic amplitude jitter, or photomechanical stochasticity, affecting wild-type and *spam* microsaccades. These results highlight that DPP microsaccades vary considerably between the flies and between individual flies' repeated

responses, suggesting that their kinematics may further reflect top-down regulation from the brain[33, 34], i.e. the flies internal state (circadian rhythm, attention or activity state)[33, 35, 36]; see also[3].

Discussion

We recorded photoreceptor microsaccades across the wild-type *Drosophila* and *spam* mutant compound eyes using a novel infrared GHS-DPP microscopy and analysed their active sampling kinematics. Remarkably, we found the *spam* mutants generating ultrafast light-induced microsaccades oriented similarly to those in the wild-type eyes. These results demonstrate that photoreceptor microsaccades are not limited to the open rhabdom eye design but can also occur in fused rhabdom eyes. Most insects, including honeybees, possess fused rhabdom eyes[30, 31], called the apposition eyes, in which phototransduction reagents, including PIP_2, are thought to function alike in *Drosophila*[37, 38]. Thus, it seems probable that all insect compound eye photoreceptors would generate active sampling. In the *spam* mutants, the microsaccades were slightly more rotated compared to the wild-type. Because *Drosophila* microsaccades follow the rhabdomere orientation along the R1-R2-R3 axis[3] (**Supplementary Video 4**), we have speculated that some structural (developmentally set) lowest resistance (energy minimum) R1-R7/8 anchoring sets the microsaccade directions[3]. Accordingly, the observed wild-type and *spam* microsaccade direction differences could reflect slight differences in their R1-R7/8 rhabdomere orientations. Unfortunately, in the circular-symmetric *spam* DPP, the separate R1-R7/8 rhabdomeres are not directly identifiable under infrared illumination. In the future, this hypothesis could be tested by expressing GFP in selected R1-R7/8 photoreceptors or rhabdomeres.

We also recorded photoreceptor microsaccades locally. In general, the *spam* DPP microsaccade displacements were smaller than the wild-type. This finding is consistent with the inter-rhabdomeric coupling hypothesis[3]. The fused rhabdom *spam* rhabdomeres embrace each other and, therefore, would have less lever to act than the open (wider-apart) wild-type rhabdomeres. Conversely, perhaps in the smaller diameter rhabdomeres, which theoretically should have smaller receptive fields[3, 39], the displacement is scaled down for an optimal active sampling (or micro-scanning) strategy. These ideas are not mutually exclusive. Both structure-function relationships could be evolutionarily tuned to scale the apposition eye photoreceptors' active sampling dynamics to each insect species' unique visual needs. For example, we would predict for fast-flying insects, having more ommatidia tiling their eyes more densely, that their photoreceptor microsaccades be smaller and faster than those of slow-flying insects of fewer less-densely-packed ommatidia. This way, a fast-eye's photoreceptor receptive fields would sample the world in higher velocity and resolution for higher visual information capture[40] - but would be metabolically more expensive[40] - than those of a slow-eye. The fast eyes should also have more frontal ommatidia with the fastest microsaccades to accentuate acuity[2] and stereoscopic range[3] than the slow-eyes.

Ultrafast microsaccades of dissociated *ex vivo Drosophila* photoreceptors show both *lateral* and *axial* components[2], implying that underneath the ommatidial lenses, light changes make photoreceptors bounce inwards and outwards and sideways in a complex piston motion[2, 3]. Both of these components shape the way how a photoreceptor encodes visual space in neural time. The axial component pulls the rhabdomere away from the ommatidium lens to collect light from a narrower angle. The lateral component makes the resulting receptive field scan the visual space. GHS-DPP microscopy produces 2D image sequences ideal for measuring the *lateral* photoreceptor microsaccade dynamics. However, the method detects less well their *axial* components, moving rhabdomeres to and from the ommatidial lens. Therefore, GHS-DPP imaging can underestimate the overall microsaccade dynamics if these show little sideways movement but have a larger (concealed) axial component.

Some sporadic interference in the measured microsaccades can originate from the intraocular muscles' activity, which exerts force on the retina. But since such muscle activity typically occurs over longer time intervals[28] or during active viewing[9], being practically absent in firmly restrained flies (see[3]), the eye muscle induced movements had little influence on the 200 ms flash experiments shown

in this report. Finally, we note that there are uncontrolled genetic differences between the two tested fly phenotypes, which could potentially contribute to their observed DPP microsaccade differences. Nevertheless, such differences would not alter the general demonstration of the fused rhabdom eye photoreceptors' active sampling as presented here.

Conclusions

Goniometric high-speed deep pseudopupil (GHS-DPP) microscopy provides an innovative non-invasive way to image photoreceptor microsaccades globally across the left and right eyes, or locally, in great detail at specific eye locations. We explained how to use it and gave out free open-source (GPLv3) software tools to quantify and compare active sampling in different insect eyes. Our results demonstrate active sampling both in open and fused rhabdom eyes. Thus, the GHS-DPP microscopy shows real potential as a powerful tool to study how the insect eyes actively sample the visual world.

Authors declare no competing interests.

Author Contributions

Conceptualization (MJ, JK, JT), Data curation (JK, NM), Formal Analysis (JK), Funding acquisition (MJ), Investigation (JK, NM, JT, MJ), Methodology (JK, JT, MJ), Project administration (MJ), Resources (MJ), Software (JK, JT), Supervision (MJ), Validation (JK, JT, MJ), Visualization (JK, MJ), Writing – main paper original draft (JK), Writing – review & editing (MJ, JK, JT).

Funding

This work was supported by Jane and Aatos Erkko Foundation Fellowships (MJ and JT), The Leverhulme Trust (RPG-2012–567: MJ), the BBSRC (BB/F012071/1, BB/D001900/1 and BB/H013849/1: MJ), the EPSRC (EP/P006094/1: MJ), the Open Research Fund of the State Key Laboratory of Cognitive Neuroscience and Learning (MJ), High-End Foreign Expert Grant by Chinese Government (GDT20151100004: MJ).

Acknowledgements

We kindly thank Andrew Zelhof for the spam fly line and Gonzalo de Polavieja, Roger C Hardie, Merlin Juusola, Gregor Belušič and the Juusola laboratory members for discussions and comments.

1 Data Availability Statement

The software code and datasets for this study can be found in the https://github.com/JuusolaLab/GHS-DPP_paper

1. Hardie, R.C. & Franze, K. Photomechanical responses in *Drosophila* photoreceptors. *Science* **338**, 260-263 (2012).
2. Juusola, M. et al. Microsaccadic sampling of moving image information provides *Drosophila* hyperacute vision. *Elife* **6** (2017).
3. Kemppainen, J. et al. Binocular Mirror-Symmetric Microsaccadic Sampling of Hyperacute 3D-Vision. *bioRxiv* (2021).
4. Agi, E. et al. The evolution and development of neural superposition. *J Neurogenet* **28**, 216-232 (2014).
5. Mahato, S., Nie, J., Plachetzki, D.C. & Zelhof, A.C. A mosaic of independent innovations involving eyes shut are critical for the evolutionary transition from fused to open rhabdoms. *Dev Biol* **443**, 188-202 (2018).
6. Zelhof, A.C., Hardy, R.W., Becker, A. & Zuker, C.S. Transforming the architecture of compound eyes. *Nature* **443**, 696-699 (2006).

7. Ahissar, E. & Arieli, A. Seeing via miniature eye movements: a dynamic hypothesis for vision. *Front Comput Neurosci* **6**, 89 (2012).

8. Donner, K. & Hemila, S. Modelling the effect of microsaccades on retinal responses to stationary contrast patterns. *Vision research* **47**, 1166-1177 (2007).

9. Franceschini, N., Chagneux, R., Kirschfeld, K. & Mucke, A. in Gottingen Neurobiology Report: Synapse - Transmission Modulation. (eds. N. Elsner & H. Penzlin) 1 (Georg Thieme Verlag, Stuttgard, New York; 1991).

10. Rucci, M., Iovin, R., Poletti, M. & Santini, F. Miniature eye movements enhance fine spatial detail. *Nature* **447**, 851-854 (2007).

11. Viollet, S. Vibrating makes for better seeing: from the fly's micro-eye movements to hyperacute visual sensors. *Frontiers in bioengineering and biotechnology* **2**, 9 (2014).

12. Land, M.F. Visual acuity in insects. *Annu Rev Entomol* **42**, 147-177 (1997).

13. Laughlin, S.B. The role of sensory adaptation in the retina. *J Exp Biol* **146**, 39-62 (1989).

14. Barlow, H.B. The size of ommatidia in apposition eyes. *J Exp Biol* **29**, 667-674 (1952).

15. Hengstenberg, R. Eye muscle system of housefly *Musca-Domestica* .1. Analysis of clock spikes and their source. *Kybernetik* **9**, 56-77 (1971).

16. Hardie, R.C. & Juusola, M. Phototransduction in *Drosophila*. *Curr Opin Neurobiol* **34**, 37-45 (2015).

17. Franceschini, N. & Kirschfeld, K. Optical study *in vivo* of photoreceptor elements in compound eye of *Drosophila*. *Kybernetik* **8**, 1-13 (1971).

18. Franceschini, N. & Kirschfeld, K. Phenomena of pseudopupil in compound eye of *Drosophila*. *Kybernetik* **9**, 159-182 (1971).

19. Franceschini, N. in Information processing in the visual systems of *Anthropods* (ed. R. Wehner) 75-82 (Springer-Verlag, Berlin, Heidelberg, New York; 1972).

20. Douglass, J.K. & Wehling, M.F. Rapid mapping of compound eye visual sampling parameters with FACETS, a highly automated wide-field goniometer. *J Comp Physiol A* **202**, 839-851 (2016).

21. Muñoz Arias, M., Douglass, J.K., Wehling, M.F. & Stavenga, D.G. Automated charting of the visual space of insect compound eyes. *arxiv* (2021).

22. Kurada, P. & O'Tousa, J.E. Retinal degeneration caused by dominant rhodopsin mutations in *Drosophila*. *Neuron* **14**, 571-579 (1995).

23. Zelhof, A.C., Koundakjian, E., Scully, A.L., Hardy, R.W. & Pounds, L. Mutation of the photoreceptor specific homeodomain gene Pph13 results in defects in phototransduction and rhabdomere morphogenesis. *Development* **130**, 4383-4392 (2003).

24. Huang, Y., Xie, J. & Wang, T. A fluorescence-based genetic screen to study retinal degeneration in Drosophila. *Plos One* **10**, e0144925 (2015).

25. Seidl, R. & Kaiser, W. Visual field size, binocular domain and the ommatidial array of the compound eyes in worker honey bees. *J Comp Physiol A* **143**, 17-26 (1981).

26. Taylor, G.J. et al. Bumblebee visual allometry results in locally improved resolution and globally improved sensitivity. *Elife* **8**, e40613 (2019).

27. Aptekar, J.W. et al. Method and software for using m-sequences to characterize parallel components of higher-order visual tracking behavior in *Drosophila*. *Front Neural Circuits* **8**, 130 (2014).

28. Hengstenberg, R. in Information Processing in the Visual Systems of Anthropods 93-96 (Springer, 1972).

29. Wardill, T.J. et al. Multiple spectral inputs improve motion discrimination in the *Drosophila* visual system. *Science* **336**, 925-931 (2012).

30. Zelhof, A.C., Hardy, R.W., Becker, A. & Zuker, C.S. Transforming the architecture of compound eyes. *Nature* **443**, 696-699 (2006).

31. Osorio, D. Spam and the evolution of the fly's eye. *Bioessays* **29**, 111-115 (2007).

32. Ready, D.F., Hanson, T.E. & Benzer, S. Development of the *Drosophila* retina, a neurocrystalline lattice. *Dev Biol* **53**, 217-240 (1976).

33. Tang, S. & Juusola, M. Intrinsic activity in the fly brain gates visual information during behavioral choices. *Plos One* **5** (2010).

34. Zheng, L. et al. Feedback network controls photoreceptor output at the layer of first visual synapses in *Drosophila*. *J Gen Physiol* **127**, 495-510 (2006).

35. van Swinderen, B. Attention-like processes in *Drosophila* require short-term memory genes. *Science* **315**, 1590-1593 (2007).

36. Fujiwara, T., Cruz, T.L., Bohnslav, J.P. & Chiappe, M.E. A faithful internal representation of walking movements in the *Drosophila* visual system. *Nat Neurosci* **20**, 72-81 (2017).

37. Fain, G.L., Hardie, R. & Laughlin, S.B. Phototransduction and the evolution of photoreceptors. *Curr Biol* **20**, R114-124 (2010).

38. Yau, K.W. & Hardie, R.C. Phototransduction motifs and variations. *Cell* **139**, 246-264 (2009).

39. Stavenga, D.G. Angular and spectral sensitivity of fly photoreceptors. II. Dependence on facet lens F-number and rhabdomere type in *Drosophila*. *J Comp Physiol A* **189**, 189-202 (2003).

40. Song, Z. & Juusola, M. Refractory sampling links efficiency and costs of sensory encoding to stimulus statistics. *J Neurosci* **34**, 7216-7237 (2014).

41. Juusola, M., Dau, A., Zheng, L. & Rien, D.N. Electrophysiological method for recording intracellular voltage responses of *Drosophila* photoreceptors and interneurons to light stimuli *in vivo*. *Jove-J Vis Exp* (2016).

42. Juusola, M. & Hardie, R.C. Light adaptation in *Drosophila* photoreceptors: I. Response dynamics and signaling efficiency at 25 degrees C. *J Gen Physiol* **117**, 3-25 (2001).

43. Gonzalez-Bellido, P.T., Wardill, T.J. & Juusola, M. Compound eyes and retinal information processing in miniature *dipteran* species match their specific ecological demands. *P Natl Acad Sci USA* **108**, 4224-4229 (2011).

44. Bradski, G. & Kaehler, A. OpenCV. *Dr. Dobb's J Software Tools* **3** (2000).

45. Virtanen, P. et al. SciPy 1.0: fundamental algorithms for scientific computing in Python. *Nat Methods* **17**, 261-272 (2020).

Methods

We describe the GHS-DPP imaging system hardware configuration, how to prepare the flies, experimental protocols, and data analysis tools and principles. All software - from recording to analysis - are available under a free and open (GPLv3) software license in a GitHub repository: https://github.com/JuusolaLab/GHS-DPP_paper.

Supplementary Videos 1-2 show how the GHS-DPP microscopy was put together and works. **Supplementary Videos 2-4** show how active sampling - by photomechanical photoreceptor

microsaccades - looks like in slow motion and how the microsaccades were analysed across the compound eyes.

Experimental setup

The GHS-DPP imaging system's two primary components are a rotation stage system and a stereomicroscope (**Fig. 2a**). The rotation system allows precise control over the fly eyes' yaw and pitch using two perpendicularly mounted rotation stages (Thorlabs PR01/M, USA), mounted horizontally and vertically. An additional small 3-axis micromanipulator, connected to the vertical rotation stage, was used to control the fly's initial position. Crucially, the vertical rotation stage further rested on a 2-axis micromanipulator so that the intersection point of the two rotation stage axes could be centred at the microscope's field of view. The rotation stage positions were acquired digitally, using two 1024-step rotation encoders (YUMO E6B2-CW23E) and an Arduino board (Arduino Uno, Italy) running a custom C++ program (**Fig. 2b**). In addition, the rotation stages were fitted with stepper motors for fully automated experiments (**Fig. 2a**). Still, in this study, the experiments were performed manually, accurately focussing on DPP at all tested eye locations. **Supplementary Video 1** shows how the GHS-DPP microscope system was put together.

The stereomicroscope was mounted sideways to function with the rotation stages. A high-intensity ultraviolet LED (UV-OptoLED, Cairn Research, UK) was inserted in the microscope's ocular slot, enabling direct light stimulation of the observed DPP rhabdomeres. This 365 nm UV-LED and the two infrared 850 nm LEDs (IR-OptoLED, Cairn Research, UK), which provided antidromic non-stimulating illumination of the DPP rhabdomeres (without activating their phototransduction) through the fly head capsule, were connected to their separate driver units (Dual OptoLED Power Supply, Cairn Research, UK). The LEDs were controlled over the BNC interface using a computer connected data acquisition system (PCI-6221 with BNC-2090A and PCI-6733 with BNC-100, National Instruments, USA) (**Fig. 2c**). The two infrared LEDs were mounted apart from each other at different angles to prevent the pipette tip or the fly body from blocking the illumination, which would otherwise frequently happen with a single point source. Both the infrared LEDs were in bespoke holders, having a convex lens with adjustable lens-to-LED distance enabled beam focusing. The second unit mounted to the microscope was the high-speed optical camera (Orca Flash 4.0 C13440, Hamamatsu, Japan), which also sent a trigger signal over the BNC interface to the data acquisition system to time the stimulus delivery precisely. We typically acquired 2,048 x 2,048 pixel full-frame images at 100 fps, and occasionally - by cropping the sensor to 2,000 x 200 pixel - collected images at 1,000 fps. The camera had a transparent infrared and opaque UV filter on its pathway, ideally stopping the UV stimulation light from reaching and polluting the image sensor (**Fig. 2d**). Besides these filters, the microscope was configured with a beam-splitter (SZX-BS, Olympus, Japan), a photo adapter piece (SZ-PHA, Olympus, Japan) and a magnification changer (U-TVCAC, Olympus, Japan).

The setup was mounted on a vibration isolation table (air table), which uncoupled any building vibrations that could affect the motion analysis results. The rotation stage system was connected to the table by magnetic clamps (Magnetic Stand, World Precision Instruments), whilst the microscope system - attached to a thick steel pole of a steel base plate - was heavy enough to ensure its fixed position. The whole setup was enclosed inside a black-painted metal cubicle, with its only open side supporting black curtains for performing the experiments in controlled, dark conditions. Accordingly, the Arduino board's few surface-mounted LEDs were covered with electrical insulation tape to minimise any light noise.

Flies and preparation

We used wild-type *Drosophila* flies (Berlin) and a fused rhabdom *spam* null-mutant line (w; *spam1/spam1* Frt; sqh-GFP/Tm6B, a gift from Andrew Zelhof) in the experiments. The flies were maintained in an incubator at 25 ℃, under a 12:12h light-dark cycle. Only healthy 3- to 20-days-old male and female flies, climbing up the vial, were selected for the experiments. We avoided using very young flies (< 3 days) because their soft heads could bulge during the imaging, presumably due to

spontaneous eye muscle activity. The flies were prepared for the experiments using the plastic pipette tip immobilisation technique[41] (**Supplementary Fig.1**). Previously, we tested a copper hook tethering technique[3], allowing simultaneous behavioural experiments (**Supplementary Fig.1a**). But because both these immobilisations gave broadly similar results[3], the more laborious and time-consuming tethering was not used here.

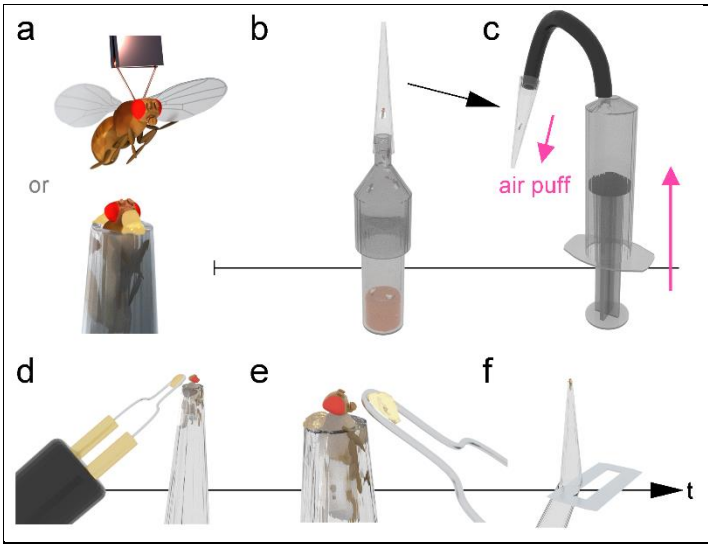

Supplementary Fig.1 | The pipette tip preparation technique. **a**, Flies can be either tethered on a small copper hook with UV-cured glue or immobilised on a plastic pipette tip with beeswax. **b**, With the help of a funnel piece, a fly was captured in a 1,000 µl plastic pipette tip. **c**, Air puffs generated by a hand-held syringe pushed the fly towards the pipette tip's small end. **d**, The fly was immobilised from its dorsal thorax. **e**, the head was secured near the proboscis using melted beeswax. **f**, The pipette excess was cut off with a razor blade, and then the preparation was inserted into the GHS-DPP imaging system.

In the pipette-tip-fixation method, a 1,000 µl plastic pipette tip was first linked to a funnel piece, and the funnel was connected to a vial full of flies. One fly at a time was lured into the pipette tip through the funnel driven by *Drosophila*'s innate geotaxis behaviour (**Supplementary Fig.1b**). This way, there was no need to immobilise the flies by CO_2 or ice-cooling that can potentially affect the microsaccades. Next, the pipette tip was viewed under a stereo preparation microscope (Olympus SZX-9, Japan). At the same time, the fly was gently pushed towards the tip opening by puffing air from a hand-held syringe (**Supplementary Fig.1c**). When needed, the pipette tip's opening was adjusted using a razor blade to ensure that the fly head passed through without any deformation, minimising structural damage to the eyes. The fly was air-puffed until its head and upper thorax protruded the tip end. When the fly was ideally positioned, it was quickly immobilised by applying melted beeswax on its thorax (**Supplementary Fig.1d**) and ventrally to its head and proboscis (**Supplementary Fig.1e**). In this correct position, the pipette would not shadow the dual-IR illumination during the experiments.

Additionally, the proboscis could have been pulled out with forceps and waxed on the pipette's outside, or the antennae waxed. However, these manoeuvres, which we often use in preparing *Drosophila* for intracellular electrophysiology[41, 42], were omitted because they made no difference in the observed microsaccades. Furthermore, these procedures would have prolonged the preparation making, potentially increasing structural damage. Conversely, some more wax was routinely applied on the dorsal side of the head, under the ocelli, to secure the head's position further. Finally, the pipette was cut from its large end using a razor blade (**Supplementary Fig.1f**), and the preparation was carefully placed in the setup (**Supplementary Video 2**).

Data acquisition and software

To enable non-specialist users to operate the GHS-DPP microsaccade imaging experiments, we created a free and open (GPLv3) recording software called *Gonio Imsoft*. *Gonio Imsoft* interfaced with the open-source microscopy software *MicroManager* to control the high-speed camera. In addition, it used the *NI-DAQmx* module (controlling the data acquisition) and the *PySerial* module (communicating with the Arduino microcontroller), reading out the rotary encoders. *Gonio Imsoft* ran on a Windows 10 platform.

We used the Olympus DF-PLAPO 1X objective for typical experiments with the microscope's continuous zoom maxed out and the additional magnification changer set to the 2x-position. In this configuration, a small-to-average-size fly head falls entirely within the field of view. The microscope's light path selector was set to its mid-state, resulting in an 80%/20% light intensity split between the camera and the eyepieces, respectively. The two infrared illumination LEDs were focused on the back of the fly head. Using the 2-axis micrometre, mounted on the horizontal rotation stage, the vertical rotation stage was centred so that the fly head, when brought to the field-of-view by the 3-axis micromanipulator (mounted on the vertical rotation stage), remained in the centre of the field of view in all possible horizontal and vertical rotation combinations (**Supplementary Video 2**). However, the microscope's focus remained only approximately correct since the fly head is not perfectly round and hence refocusing was needed to maintain a sharp DPP image during the experiments.

The microscope was first focused so that the ommatidial lenses appeared crisp and clear. Then, the focus was brought deeper into the eye until the DPP became clear and visible. In this ommatidial axes' converge point, images formed by individual ommatidia superimpose, creating a magnified, virtual image of the rhabdomere tips[18]. Using our computer graphics (CG) simulations on wild-type and *spam* eyes, we further confirmed that the retinal patterning (**Fig. 1a** and **b**) indeed resulted in a one-spot DDP image in the *spam* (**Fig. 1c**).

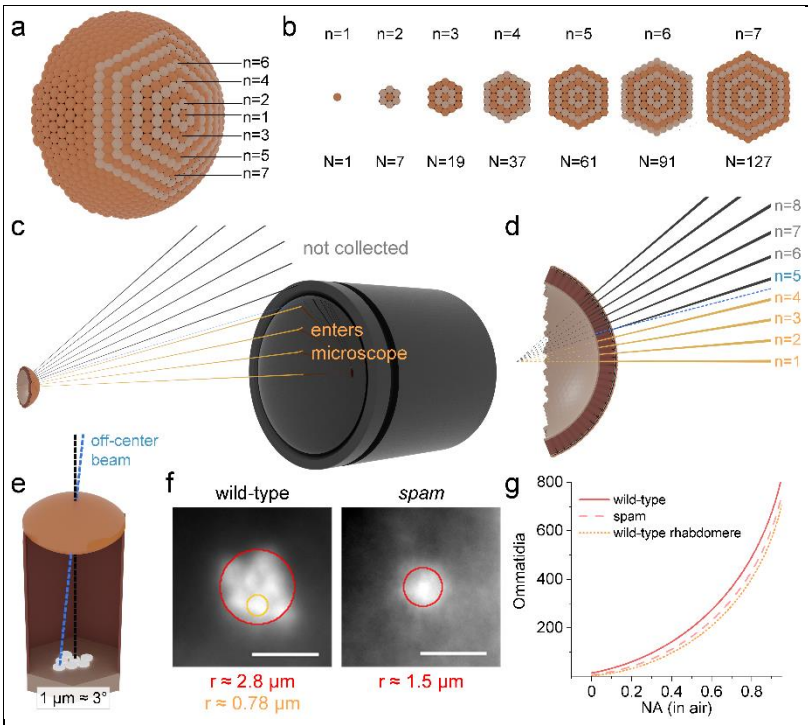

Supplementary Fig. 2 | The amount of DPP forming ommatidia depends on the microscope numerical aperture. **a**, A spherical compound eye illustrated with seven centred hexagonal rings. **b**, The *n*th centred hexagonal number quantifies the number of ommatidia, N, within the *n*th ring. **c**, Light rays emerging from the retina midpoints can be collected by the microscope only if their incident angle is smaller than the microscope's half-collection angle, *Θ*. **d**, Some light from the uncollected ommatidia may reach the microscope if it originates off-centre (blue). **e**, light originating 1 µm off-centre is approximately 3° diverted compared to the optic axis. **f**, The *r* parameters were estimated from the wild-type and *spam* DPPs, and one wild-type DPP rhabdomere. The scale bar corresponds to 50 µm in the DPP images and 5 µm physically in the retina. **g**, The amount of DPP forming ommatidia (here *c*=0) rises sharply with the increasing microscope numerical aperture, NA.

The DPP is purely an optical phenomenon, informing us more about how the observed rhabdomere summation image is affected by the used microscope system[18] than how the fly compound eye converges visual inputs from the world[34]. Therefore, the DPP cannot tell us too much about the eyes' neural superposition design, in which R1-R6 photoreceptor outputs from six neighbouring ommatidia, sampling light over the same small visual area, are synaptically pooled. Nevertheless, it is helpful to estimate the number of ommatidia forming in the optical DPP image as this improves our understanding of any blurring and irregularities in it. On a hexagonal tiling, the number of hexagons

within an *n*th concentric hexagonal circle (**Supplementary Fig. 2a** and **b**) can be calculated using the formula

$$\begin{cases} N = 3n(n-1)+1 & \text{if} \quad n \geq 1 \\ N = n & \text{if} \quad n < 1 \\ N = 0 & \text{if} \quad n \leq 0 \end{cases} \tag{1}$$

The values of *N* are known as the centred hexagonal numbers. The piecewise formulation also accounts for the $n < 1$ cases, which are normally left undefined. By finding the right *n,* we use it to denote the number of ommatidia participating in the DPP image formation. From the eye-microscope geometry (**Supplementary Fig. 2c** and **d**), we can estimate the value of *n,* after which the illumination light rays no longer can enter the microscope's entrance pupil, and write

$$n = \frac{\theta + 2(0.5-c)\alpha}{\Delta\varphi} + 1 \tag{2}$$

θ is the half-angle subtended by the microscope lens to the eye, $\Delta\varphi$ is the interommatidial angle, c is the minimum counted contribution term and α is the mean deviation angle between the outermost rhabdomere receptive axes and the ommatidial axis. If we were to estimate the number of ommatidia that project all their rhabdomeric light to the microscope, $c = 1$, and conversely, if we were interested in ommatidia casting *any* rhabdomeric light to the microscope, $c = 0$. For counting ommatidia with other contributions, the correct c depends on the microscope NA. But for a 50% minimum contribution estimate, we can use the former estimates. Then next, ideally, if the rhabdomeres formed a single point on the ommatidial axis (and the eye was perfectly spherical), α would be zero. And, if the rhabdomeres were organised into a hexagonal shape so that the neighbouring rhabdomeres' receptive fields (RFs) perfectly overlap at infinity, α would nearly equal the interommatidial angle $\Delta\varphi$.

By replacing the half-angle with the numerical aperture (NA) and considering that in *Drosophila* 1 µm displacement results in a 3° angular change[3], we can write

$$n = \frac{\sin^{-1}\left(\frac{NA}{m}\right) + 2(0.5-c)\,(3^{\circ}/\mu\text{m}\ r)}{\Delta\varphi} + 1 \tag{3}$$

NA is the numerical aperture of the used microscope, m is the refractive index of microscope objective immersion medium (m = 1 for air), and r is the radius of a circle in the ommatidial retinal plane that representatively contains all the rhabdomeres. The numerical aperture in our microscope system was 0.11, and the *Drosophila* interommatidial angle is approximately 5° [39, 43]. Since the DPP image is a ~10x magnified image of the rhabdomere tips, the r parameters for the wild-type and *spam* can be estimated directly from the DPP still images as 2.8 µm and 1.5 µm (**Supplementary Fig. 2f**). Inserting these values in (3) and then calculating (1), we approximate that in our microscope system, 18 ommatidia would contribute at least 50% to the deep pseudopupil image formation in the wild-type and 12 ommatidia in the *spam* eye. For one rhabdomere in the wild-type DPP pattern, we can similarly estimate that its *r* is 0.78 µm (**Supplementary Fig. 2f**), suggesting that 10 ommatidia form it. Notice, however, that because of the structural asymmetricities, these ommatidium counts are likely slightly overestimated. For example, the *Drosophila* ommatidial R1-R6 rhabdomeres are not hexagonally arranged around the lens centre. Instead, their sizes and distances vary[2], forming an asymmetric (slanted) trapezoid arrangement (**Fig. 3c**), and the eye is not perfectly spherical. Moreover, infrared illumination, by passing through the ommatidial screening pigments that block non-axial green and UV transmission, could potentially merge more ommatidia into the DPP image than visible light. Nevertheless, since these upper-bound estimates vary with the used microscope systems (**Supplementary Fig. 2g**), we calculated them for a range of air-objective NAs (**Supplementary Table 1**).

Table. The estimated number of ommatidia forming the DPP image

Microscope NA (in air)	N (wild-type ommatidia) (r = 2.8 µm)			N (*Spam* ommatidia) (r = 1.5 µm)			One wild-type rhabdomere (r = 0.78 µm)		
	contributing at least								
	100%	50%	>0%	100%	50%	0%	100%	50%	>0%
0.001	0	7.3	15	0.11	3.2	6.2	0.54	1.8	3.1
0.01	0	8.0	16	0.21	3.7	7.1	0.65	2.2	3.8
0.05	0	11	23	0.67	6.3	12	1.3	4.4	7.4
0.1	0.47	17	33	1.9	11	20	4.4	9.1	14
0.2	4.1	32	61	11	26	41	17	25	32
0.4	38	90	143	56	84	112	68	83	97
0.6	115	195	274	146	189	231	165	187	209
0.8	268	380	492	314	374	434	341	372	403
0.95	521	671	821	585	665	745	622	663	705

In this study, we performed two kinds of experiments: *local recordings* at a fixed position on the left and right eye and *global recordings* across the eyes. In the local recordings, we imaged one location on the left eye (+28° horizontal and -37° vertical) and another on the right eye (-28° horizontal and -37° vertical) because, at these locations, the upper infrared LED illuminated the eyes ideally, forming the crispest DPP. The stimulus UV-LED was flashed for 200 ms while simultaneously the high-speed camera acquired images 100 frames per second, yielding 20 image frames per flash. As a standard procedure, this recording process was repeated 25 times to obtain the mean photoreceptor microsaccade estimates and inspect their variability in an individual fly. Between the repeats, we initially used 10 s inter-stimulus-interval (ISI) for both the wild-type and spam flies. But ISI was later shortened ISI to 2 s, as there was no significant reduction in the response amplitude. All images were saved as 16-bit unsigned-integer, grayscale TIFF images.

The global imaging procedure was similar, but it was performed only once at each location. Instead, after each flash, the fly was rotated in 10° steps from -40° to +50° (limited by the vertical rotation stage, covering the microscope objective or the two illumination LEDs) using the horizontal rotation stage. After completing the horizontal "line scan", the vertical rotation stage was advanced in a 10° step, covering a range from -110° to +110°. By rotating the fly and imaging in between, we scanned approximately 200 distinct locations on the left and right eyes. Overall, it took about 10 s to reorient the fly, refocus at the deep pseudopupil and start the image acquisition protocol again.

Data analysis

To quantify the 3-dimensional rhabdomere movement fields, we created a free and open (GPLv3) data analysis software called *Gonio Analysis*. It allows drawing regions of interest (ROIs) around the deep pseudopupil, performing motion analysis, and finally, translating the motion results from the camera image coordinates to the fly's 3D frame-of-reference, using the digitally read rotation stage values. Here, we shortly describe its data analysis principles.

Rectangular ROIs were drawn by hand for the first frame of each location only by selecting the deep pseudopupil. Next, these pseudopupil images were used as template images for cross-correlation based motion analysis (**Supplementary Fig. 3a**). We used the computer vision library *OpenCV* [44] and its *matchTemplate* routine for the following 2D cross-correlation

$$R(x,y) = \frac{\sum_{x',y'}(T'(x',y')\, I'(x+x',y+y'))}{\sum_{x',y'} T'(x',y')^2 \sum_{x',y'} I'(x+x',y+y')^2} \quad (4)$$

$$T'(x',y') = T(x',y') - \frac{1}{w*h} * \sum_{x',y'} T(x'',y'') \quad (5)$$

$$I'(x+x',y+y') = I(x+x',y+y') - \frac{1}{(w*h)} * \sum_{x'',y''} I(x+x'',y+y'') \quad (6)$$

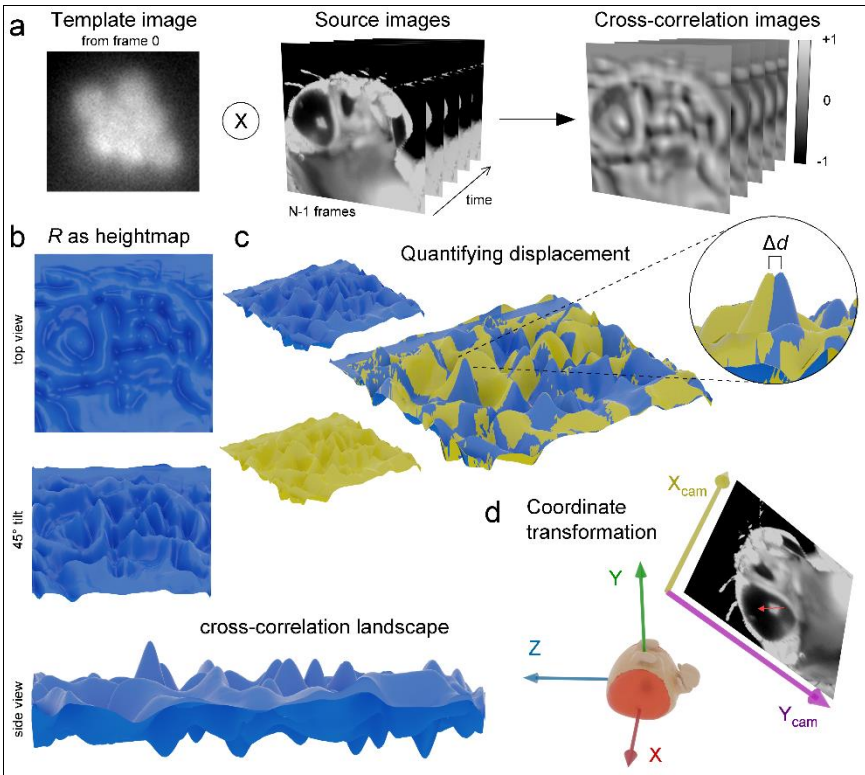

Supplementary Fig. 3 | Cross-correlation based motion analysis by template matching. **a**, The first frame of the DPP image, manually cropped, was used as the template image. By 2D cross-correlation analysis, the DPP image locations were searched among the source images. **b**, A cross-correlation result image *R* can be presented as a height-map, giving a better view of the cross-correlation landscape. **c**, Two superimposed R height-maps reveal a small shift Δd in the location of the primary maxima; This is the DDP displacement. **d**, The motion analysis results were transformed from the camera image coordinates to the fly coordinate system using the rotation stage values.

R is the 2-dimensional cross-correlation image, and $R(x,y)$ is its value at the pixel (x,y). x', x'' and y', y'' are summation indices within ranges $[0, 1, 2, \ldots, w\text{-}1]$ and $[0, 1, 2, \ldots, h\text{-}1]$, w and h are the width and height of the template image. I is the source image, and T is the template image.

In the cross-correlation results of the images R produced by the template matching (**Supplementary Fig. 3b**), the higher values were signed for the higher similarity between the template and source images at each location. Therefore, using two source images acquired at different times, the template displacement between these images can be calculated by comparing their resulting cross-correlation image's peak values (**Supplementary Fig. 3c**). Furthermore, we visually confirmed some of the motion analysis results by creating videos in which the rectangular ROI box was moved according to the motion analysis results, readily following the moving DPP. On the other hand, we note that computing the complete cross-correlation with uncropped source images (cf. **Fig. 1**) is inefficient and can lead to a false match. Therefore, we instead performed the cross-correlation only in the near vicinity (30 pixels) of the DPP cropping without truncating the responses.

In the template matching, the motion analysis results were given in the camera image coordinates. To translate them from the camera system to the 3D space in the fly's frame of reference (**Supplementary Fig. 3d**), we used the digitally read vertical *v* and horizontal *h* rotation stage values on the following set of equations

$$\begin{cases} y = \cos(h)\cos(v) \\ z = y\tan(v) \\ |x| = \sqrt{1-y^2-z^2} \end{cases} \quad (7)$$

to calculate the microscope's (x, y, z) location. Using the same equation set, in short, $P(h, v) \rightarrow (x, y, z)$, we then calculated the camera x unit vector as the vector from $P(h, v)$ to a slightly displaced point $P(h + \Delta h, v)$

$$\hat{\imath}_{cam}(h, v) = \overrightarrow{P(h, v)\, P(h + \Delta h, v)} \tag{8}$$

where Δh is ideally as small as possible but large enough not to cause errors because of limited floating-point precision. Since the y-camera-unit only depends on the vertical rotation and its x-component in the fly coordinate system is conveniently zero (i.e. the y-unit-vector is always perpendicular to the great circle arc that the microscope travels along from the fly's point of view), it is simply

$$\hat{\jmath}_{cam}(v) = -\sin(v)\,\hat{\jmath} + \cos(v)\hat{k} \tag{9}$$

Finally, the (x, y, z) movement vectors can be then calculated using camera unit vectors as

$$\boldsymbol{v}(m_x, m_y, h, v) = m_x \hat{\imath}_{cam} + m_y \hat{\jmath}_{cam} \tag{10}$$

where m_x and m_y are the camera image x and y movement values produced by the cross-correlation.

We averaged the results over many flies using simple N-nearest neighbour interpolation for the microsaccade vector maps acquired in the global recordings. For each interpolation point, from each of the N imaged flies, the nearest 3D vector was selected, but only if the angular distance of the 3D vector was not larger than 2-times the angular interpolation step of 5°. And, these equal or less than N vectors were averaged together only if there were N/2 of them or more. The difference in the wild-type and *spam* vector maps were calculated point-wise as

$$e(\boldsymbol{v_{wtb}}, \boldsymbol{v_{spam}}) = \frac{1}{\pi} \cos^{-1}\left(\frac{\boldsymbol{v_{wtb}} \cdot \boldsymbol{v_{spam}}}{\|\boldsymbol{v_{wtb}}\|\|\boldsymbol{v_{spam}}\|}\right) \tag{11}$$

where $\boldsymbol{v_{wtb}}$ and $\boldsymbol{v_{spam}}$ are the microsaccade vectors and the operators $\cdot$ and $\|\ \|$ denote the inner product and the vector norm, respectively. Finally, for rotation direction analysis, we rotated the vectors on the x-axis and calculated whether the spam vectors were rotated clockwise or counterclockwise compared to the wild-type and then used this result to sign the error in (11).

In the local recordings, we focused solely on the directionless microsaccade magnitude, calculated using the Pythagorean theorem from the camera coordinate movement values. From the mean magnitude or displacement trace, we calculated the mean and used the mean for the total displacement, speed, logistic growth factor and half-rise time quantifications. The probability graphs were calculated as 1D-histograms at each time point, with 20 stitched together to cover the whole imaging period. The total displacement values were quantified from the magnitude data by simply taking the mean of the last 7 data points; that is, the last 70 ms of the imaging. The maximum speed was calculated from the highest value between frames displacement. For the logistic growth factor and the half-rise time, we fitted the data with the sigmoidal logistic function

$$f(t) = \frac{L}{1 + e^{-k(t - t_0)}} \tag{12}$$

where L is the maximum value corresponding to the total rhabdomeric displacement, k is the logistic growth factor that in our case characterises the microsaccade activation phase time-duration, and t_0 is the half-rise time.

Statistical tests

All the quantified local recording parameters (displacement, speed, growth factor and rise-time) appeared reasonably normally distributed. However, since the wild-type sample size was 3-times larger than the *spam* one, we used Welch's t-test[45] that performs better with uneven samples for all comparisons.